Nano Research
2022, 15(8): 7063–7070

ISSN 1998-0124 CN 11-5974/O4
https://doi.org/10.1007/s12274-022-4377-4

Research Article

N-doped carbon dots coupled NiFe-LDH hybrids for robust electrocatalytic alkaline water and seawater oxidation

Peng Ding, Haoqiang Song, Jiangwei Chang (✉), and Siyu Lu (✉)

Green Catalysis Center, and College of Chemistry, Zhengzhou University, Zhengzhou 450000, China

Received: 8 February 2022 / **Revised:** 12 March 2022 / **Accepted:** 30 March 2022

ABSTRACT

Electrolysis of seawater offers a highly promising and sustainable route to attain carbon-neutral hydrogen energy without demanding on high-purity water resource. However, it is severely limited by the undesirable chlorine oxidation reaction (ClOR) on the anode and the releasing toxic chlorine species, inducing anode corrosion and multiple pollutions to reduce the efficiency and sustainability of this technology. The effective way is to limit the overpotential of oxygen evolution reaction (OER) below 480 mV and thus suppress the ClOR. Herein, we demonstrate that nitrogen-doped carbon dots strongly coupled NiFe layered double hydroxide nanosheet arrays on Ni foam (N-CDs/NiFe-LDH/NF) can efficiently facilitate OER with an ultralow overpotential of 260 mV to deliver the geometric current density of 100 mA·cm^{-2} and a Tafel slope of as low as 43.4 mV·dec^{-1} in 1.0 M KOH. More importantly, the N-CDs/NiFe-LDH/NF electrode at 100 mA·cm^{-2} shows overpotentials of 285 and 273 mV, respectively, by utilizing 1.0 M KOH with 0.5 M NaCl and 1.0 M KOH with 1.0 M NaCl as the simulated seawater, well avoid triggering ClOR. Notably, despite the complex environment of real seawater, N-CDs/NiFe-LDH/NF still effectively promotes alkaline seawater (1.0 M KOH + seawater) electrolysis with a lifetime longer than 50 and 20 h, respectively, in 1.0 M KOH and alkaline seawater electrolytes. The investigation result reveals that M–N–C bonding generated between N-CDs and NiFe-LDH intrinsically optimizes the charge transfer efficiency, further promoting the OER kinetics.

KEYWORDS

N-doped carbon dots, electrocatalysis, oxygen evolution reaction (OER), seawater oxidation, chlorine oxidation reaction (ClOR)

1 Introduction

With the increasing concern about the global energy crisis, and ecological issues, the development of the renewable energy conversion technologies for the production of hydrogen fuels has gained much attention and become the research top [1–5]. Among them, electrocatalytic water splitting is one of the most promising and matured alternative for the large-scale hydrogen generation in terms of low cost, high processing efficiency, long lifetime, and carbon neutrality [6–11]. However, the current water electrolysis technology still highly depends on the feed of high-purity fresh water, which largely hinders its commercial development in various environment, such as arid, steppe, on- or off-shore areas [12]. In this view, seawater electrolysis has been attracting continuously increasing attention because of the inexhaustible reserves of ocean (occupying about 96.5% of the water reserve on the earth). However, the intricate ionic chemistry of seawater brings great difficulty in dealing with ionic diffusion, side reactions, and anode corrosion/poison during the electrolysis of seawater [13]. Actually, the most notorious obstacle to seawater electrolysis under alkaline conditions is the competitive reaction between the oxygen evolution reaction (OER, $4OH^- \rightarrow O_2 + 2H_2O + 4e^-$, 1.23 V vs. reversible hydrogen electrode (RHE)) and the chlorine oxidation reaction (ClOR, $Cl^- + 2OH^- \rightarrow ClO^- + H_2O + 2e^-$, 1.72 V vs. RHE) on the anode owing to their similar thermodynamic potential, and the latter will decrease the Faradaic efficiency of OER and produce chlorine-containing species (e.g., ClO^-, Cl_2, etc) to chemically etch electrode [14, 15]. Theoretical studies show that the chemical potential between OER and ClOR will be maximized, with a difference in oxidation potential reaching about 480 mV, which means that when the extra overpotential (η) of is less than 480 mV at a certain geometric current density, the ClOR process will be thermodynamically inhibited to achieve 100% seawater electrolysis [16, 17]. Additionally, another crucial challenge of seawater electrolysis that inorganic and organic microorganisms can cause catalyst poisoning cannot be ignored [18]. Accordingly, rationally design catalyst is imperative to provide high-efficiency OER activity for seawater electrolysis in a mild electrochemical environment.

NiFe layered double hydroxide (LDH) has been favored by researchers because of that their tunable layered and electronic structures can be tuned to optimize the catalytic activity [19, 20]. Nevertheless, the intrinsically poor electrical conductivity and limited specific surface area of NiFe-LDH hinder the further improvement of performance in OER [21–23]. Selective building heterostructure in NiFe-LDH for efficient utilization of each individual component is considered as a promising approach to design OER catalyst [24, 25]. Carbon dots (CDs) are a class of quasi-zero-dimensional semiconducting nanomaterials with carbon as the backbone, composed of extremely small-sized spherical or quasi-spherical carbon particles (below 10 nm), and

Address correspondence to Jiangwei Chang, jwchang2021@zzu.edu.cn; Siyu Lu, sylu2013@zzu.edu.cn

possess excellent properties such as superior electron transfer ability, abundant edge defects and easy modification, which are beneficial to facilitate the design of CDs-based advanced energy materials [26–29]. Therefore, the diversity of properties makes CDs very promising precursors for the preparation of multifunctional electrode materials in electrocatalysis [30, 31]. In addition, heteroatom doping in CDs endows strong and intimate metal–carbon interactions, which tightly binds nanocarbons to metal particles, single metal atoms or nanoalloys, enhancing the catalyst stability against the dissolution and corrosion [32]. More importantly, the simultaneously generated carbon–metal bonding architecture would offer effective mass transport features, which is profitable to boost the OER activities at the atomic level for the carbon-based catalysts [33]. In this regard, it is well expected that the uniform integration between N-doped CDs (N-CDs) and NiFe-LDH can create abundant interface to enhance the synergetic effects, which facilitate high exposure and dispersion of catalytic active sites and enable fast mass transfer at high current densities, thus exhibiting excellent OER performance.

Herein, N-CDs strongly coupled NiFe-LDH *in situ* grown on Ni foam (N-CDs/NiFe-LDH/NF) was proposed as highly efficient catalyst to facilitate electrocatalytic seawater oxidation. Benefiting from the high exposure of metal active sites, the M–N–C bonding produced by hybridization and optimized electronic structures in composite components, the N-CDs/NiFe-LDH/NF electrode exhibits superior performance for OER with low overpotentials of 260 and 273 mV, respectively, to deliver the current density of 100 $mA{\cdot}cm^{-2}$ in 1.0 M KOH and simulated seawater, which well avoids triggering ClOR. Impressively, the electrode performs well even in the complex environment of alkaline seawater. Also, N-CDs/NiFe-LDH/NF shows good durability within 50 and 20 h in 1.0 M KOH and alkaline seawater, respectively. This work presents a novel route toward the rational design of the advanced transition metal-carbon hybrid catalysts and especially, promotes the wide applications of CDs-based functional materials in the green and renewable energy technologies.

2 Experimental

2.1 Preparation of N-CDs

Typically, 1.0 g of ethylenediamine and 16 mmol of citric acid were added to 30 mL of ultrapure water, and then it was transferred to an autoclave and heated at 200 °C for 8 h. After natural cooling of the reaction system to room temperature, the obtained solution was centrifuged to remove the sediment. Then, the CDs solution was lyophilized for 2 days to obtain the required samples.

2.2 Preparation of N-CDs/NiFe-LDH/NF and NiFe-LDH/NF

The N-CDs/NiFe-LDH/NF was prepared by a hydrothermal method. At first, a piece of nickel foam (NF, 1 cm × 6 cm) was treated with ultrapure water, acetone, and ethanol by ultrasonic treatment. Subsequently, 0.56 g $Ni(NO_3)_2{\cdot}6H_2O$, 0.111 g $Fe(NO_3)_3{\cdot}9H_2O$, 0.6 g urea, 0.148 g NH_4F, and different amount of N-CDs (8, 16, 24, 32, and 40 mg, corresponding to N-CDs/NiFe-LDH/NF-*X*, *X* = 0.1, 0.2, 0.3, 0.4, and 0.5 $mg{\cdot}mL^{-1}$ N-CDs) were dissolved into 40 mL ultrapure water under continuously vigorous stirring to form a clear solution. Then, the above solution was transferred to the autoclave with a piece of pretreated NF and heated at 120 °C for 5 h. Finally, the obtained samples were washed by centrifugation and vacuum dried at 70 °C for 3 h to obtain N-CDs/NiFe-LDH/NF-*X*. NiFe-LDH/NF was also prepared by the similar way to that of N-CDs/NiFe-LDH/NF-*X* without the adding of N-CDs.

2.3 Preparation of RuO_2/NF

A mixture of 10 mg RuO_2, 40 μL Nafion, 720 μL ethanol, and 240 μL ultrapure water were sonicated for 10 min. Then, the active material was coated on the pretreated NF surface. Finally, the electrode was removed and placed on filter paper to dry at room temperature.

2.4 Preparation of N-CDs/NF

At first, 1.0 g of ammonium citrate was added to 40 mL of ultrapure water under continuously vigorous stirring for 30 min. Subsequently, the solution was transferred to a stainless-steel autoclave containing a piece of prepared NF, and heated at 180 °C for 2 h. Finally, the samples were washed by centrifugation and dried under vacuum for several hours.

2.5 Preparation of alkaline seawater

0.68 g Na_2CO_3 was added into 100 mL natural seawater to effectively precipitate Mg^{2+} and Ca^{2+} cations, after which the supernatant was collected for preparing the 1 M KOH seawater electrolyte. Therefore, no $M(OH)_2$ (M = Ca/Mg) formed on the electrode during the electrolysis of seawater OER. Na_2CO_3 is less expensive than KOH, making it a reasonable chemical to treat the natural seawater in the electrolyte-preparation process.

2.6 Characterization

In the Electronic Supplementary Material (ESM), details of the instruments used to characterize the material are described.

2.7 Electrochemical measurements

Electrochemical tests were carried out via a CHI 660E potentiostat in a standard three-electrode setup composing of working electrode, the counter electrode, and the reference electrode. The OER activity was assessed utilizing linear sweep voltammetry (LSV, 5 $mV{\cdot}s^{-1}$). The tests were performed in 1.0 M KOH solution, simulated seawater (1.0 M KOH + 0.5 M/1 M NaCl) and alkaline seawater (1.0 M KOH + seawater). All the potentials were displayed versus RHE by: E (vs. RHE) = E (vs. SCE) + 0.0591 × pH + 0.241. The 100% infrared (iR)-corrected was applied to corresponding electrochemical data.

2.8 OER multi-step reaction process (alkaline environment)

$$4OH^- \rightarrow {}^*OH + 3OH^- + e^- \quad (1)$$

$$^*OH + 3OH^- \rightarrow {}^*O + H_2O + 2OH^- + e^- \quad (2)$$

$$^*O + 2OH^- + H_2O \rightarrow {}^*OOH + H_2O + OH^- + e^- \quad (3)$$

$$^*OOH + OH^- + H_2O \rightarrow O_2 + 2H_2O + e^- \quad (4)$$

where * represent the adsorption point on the catalyst surface.

2.9 Electrochemically active surface area (ECSA) normalization

The geometric model used to estimate the surface area of the catalyst suffers from large errors. Therefore, this work will employ ECSA normalization to calculate the intrinsic activity of the catalyst.

ECSA was measured by cyclic voltammetry (CV) in the nonfaradaic region (at potentials where charge transfer reactions do not occur but adsorption and desorption processes occur)

$$\mathrm{ECSA} = \frac{C_{\mathrm{dl}}}{C_{\mathrm{s}}} \quad (5)$$

where C_{dl} is the double layer capacitance; C_{S} is the specific capacitance.

ECSA normalization

$$j_{\mathrm{ECSA}} = \frac{j}{\mathrm{ECSA}} \quad (6)$$

where j is the current density with iR-compensation.

In order to simplify the calculation process, the intrinsic activity of the catalyst will be calculated by the following formula

$$\text{Intrinsic activity} = \frac{j}{C_{\mathrm{dl}}} \quad (7)$$

2.10 Calculation of turnover frequency (TOF)

TOF is defined as the number of turnovers of a single active site per unit time, as a measurement of the intrinsic activity of the catalyst. For OER, TOF value is derived using the following formula

$$\mathrm{TOF} = \frac{j \times A}{4 \times N \times F} \quad (8)$$

where j means as sate above. A is the geometric surface area of NF electrode (0.5 cm × 0.5 cm). F is Faraday's constant. N is the molar number of active site. According to previous studies, Ni is defined as the active site, and the number is estimated by the following method

$$N_{\mathrm{ECSA}} = \frac{\mathrm{ECSA} \times C_{\mathrm{cell}}}{V_{\mathrm{cell}} \times N_{\mathrm{A}}} \times n_{\mathrm{cell}} \quad (9)$$

In this equation, ECSA is the electrochemical surface area, V_{cell}, C_{cell}, and n_{cell} are the volume of the unit cell, the c axis length of the unit cell, and the number of metal atoms per unit cell, respectively. For NiFe, the crystal structure of NiOOH[12] was used as the model structure, in which V_{cell} = 47.41 Å^3, C_{cell} = 6.88 Å (interlayer spacing of the layered double hydroxide) and n_{cell} = 1 Ni atoms per unit cell [34, 35].

3 Results and discussion

The N-CDs/NiFe-LDH/NF with bridged structures, where uniformly dispersed CDs are connected to NiFe-LDH by M–N–C bonds, are schematically exhibited in Fig. 1(a). The phase composition and morphology of N-CDs/NiFe-LDH/NF were carefully investigated. The X-ray powder diffraction (XRD) patterns of N-CDs/NiFe-LDH in Fig. 1(b) show some clear diffraction peaks, which are matched with the (003), (006), (101), (012), (015), (018), (110), and (113) crystal planes of NiFe-LDH (JCPDS No. 40-0215), indicative of the successful synthesis of the NiFe-LDH phase in N-CDs/NiFe-LDH. The carbon peak, as can be seen from the pattern of N-CDs, was not detected in N-CDs/NiFe-LDH and it may be attributed to its poor crystallization and low content in compared with metal species (Fig. S1 in the ESM). In addition, it can be observed that the smooth surface of pure NF (Fig. S2 in the ESM) was covered with crisscross N-CDs/NiFe-LDH nanosheet arrays to form a complete self-

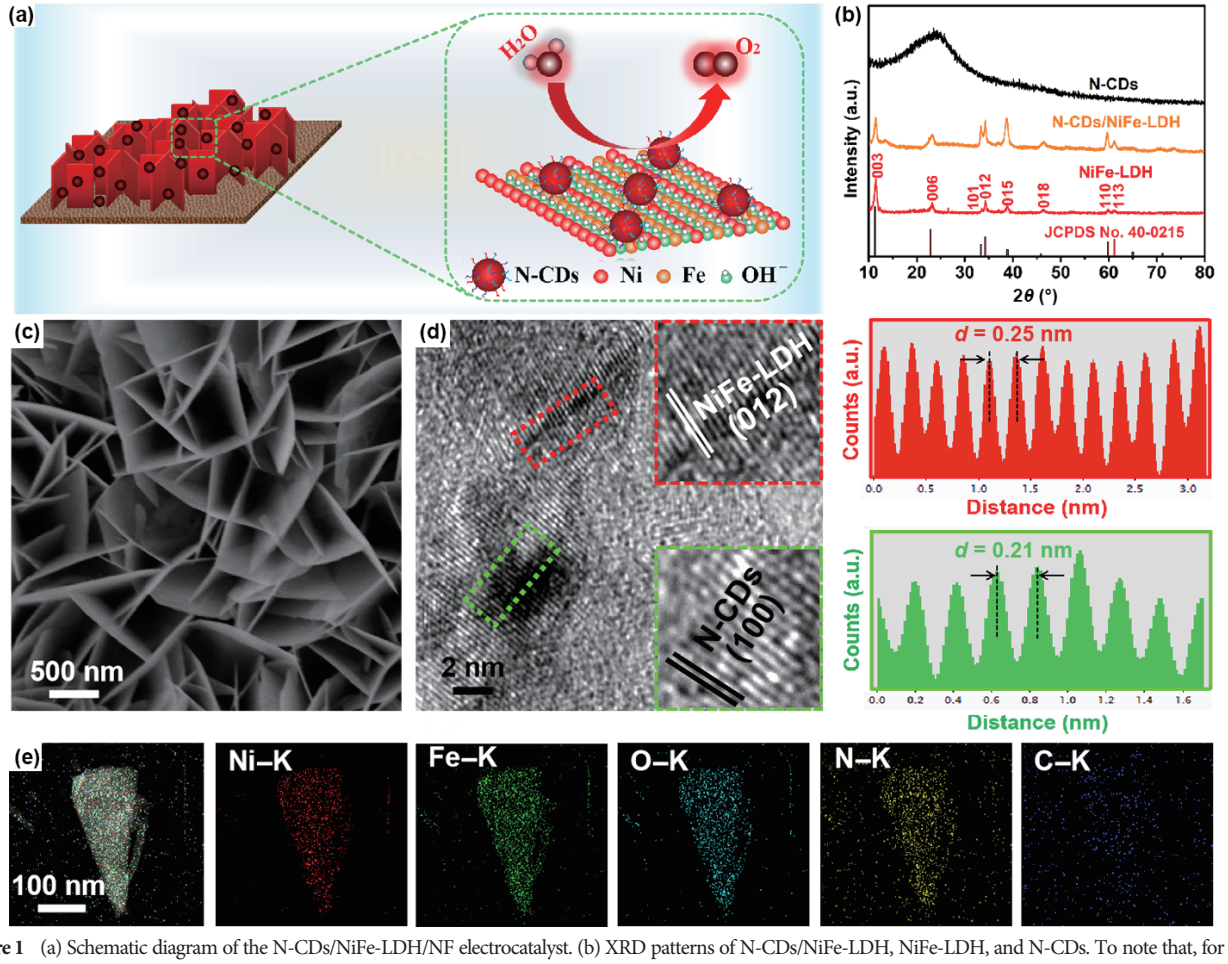

Figure 1 (a) Schematic diagram of the N-CDs/NiFe-LDH/NF electrocatalyst. (b) XRD patterns of N-CDs/NiFe-LDH, NiFe-LDH, and N-CDs. To note that, for more qualitative analysis of the crystalline species, N-CDs/NiFe-LDH is scrapped from the N-CDs/NiFe-LDH/NF to avoid the influence of NF. (c) High-magnification SEM images of N-CDs/NiFe-LDH/NF. (d) HRTEM images of N-CDs/NiFe-LDH. Insets to the right exhibit the intensity profiles for NiFe-LDH and N-CDs, as labelled with red and green dashed boxes. (e) TEM and the corresponding EDX elemental mapping images of N-CDs/NiFe-LDH.

supporting electrode, as shown in Fig. 1(c) and Fig. S3 in the ESM. Further analysis from the transmission electron microscope (TEM) and the high-resolution TEM (HRTEM) images (Fig. 1(d) and Fig. S4 in the ESM) reveals the ultrathin lamella property and distribution of N-CDs of the as-prepared sample, and N-CDs are embedded on the surface of NiFe-LDH can be clearly observed. Furthermore, HRTEM image confirmed that the nanosheet arrays are well crystallized with a lattice spacing of 0.25 nm, which is a signal of the (012) plane of NiFe-LDH. Also, the CDs with an interlayer spacing of 0.21 nm, attributed to the (100) plane of carbon [36], can be observed. Energy-dispersive X-ray (EDX) elemental mapping in Fig. 1(e) displays that the Ni, Fe, O, N, and C elements are uniformly distributed over N-CDs/NiFe-LDH, further supporting the above discussions. As illustrated in Table S1 in the ESM, the atomic ratio of Ni-to-Fe is approximately 7:1 measured by inductively coupled plasma-mass spectrometry (ICP-MS), which is consistent with the feeding ratio. For comparison, NiFe-LDH *in situ* grown on NF without N-CDs (NiFe-LDH/NF) and different amounts of N-CDs loaded on NiFe-LDH (N-CDs/NiFe-LDH/NF-*X*) were also synthesized under the same hydrothermal conditions, as exhibited in detail in Figs. S5 and S6 in the ESM.

To identify the elemental compositions and the chemical environments, as well as the changes of electronic structure, the N-CDs/NiFe-LDH and NiFe-LDH samples were characterized by X-ray photoelectron spectroscopy (XPS). The XPS survey spectrum in Fig. S7(a) in the ESM shows the distribution of Ni, Fe, N, C, and O elements in N-CDs/NiFe-LDH. As exhibited in Fig. 2(a), the two major peaks at 874.0 and 856.2 eV in the Ni 2p region of N-CDs/NiFe-LDH can be attributed to the typical signals of Ni $2p_{1/2}$ and Ni $2p_{3/2}$, respectively, along with two shakeup satellite peaks (marked as "Sat.") at 880.0 and 862.1 eV, verifying the coexistence of Ni^{2+} and Ni^{3+}. Impressively, compared with that of NiFe-LDH, the binding energies of Ni $2p_{1/2}$ and Ni $2p_{3/2}$ peaks in N-CDs/NiFe-LDH exhibit positive shift of 1.28 and 1.12 eV, respectively, demonstrating the electron transfer from metal sites to N-CDs. For the Fe 2p region in Fig. 2(b), two typical peaks at 724.8 and 712.9 eV are matched with Fe $2p_{1/2}$ and Fe $2p_{3/2}$, respectively. The peaks (Sat.) located at 721.0 and 736.4 eV are consistent with Fe^{2+}/Fe^{3+} ions in iron hydroxide. Similarly, the binding energies of Fe $2p_{1/2}$ and Fe $2p_{3/2}$ peaks in N-CDs/NiFe-LDH show the positive shift of 1.0 and 0.29 eV, respectively, compared to that of NiFe-LDH, indicative of that electron transfer from metal sites to N-CDs. In addition, the N 1s region in Fig. 2(c) shows three characteristic peaks of N-CDs, namely, oxidized-N (403.5 eV), pyrrolic-N (401.0 eV), and pyridinic-N (399.0 eV). More importantly, it should be noted that a prominent peak for M–N–C (M = Ni or Fe) bond appears at 400.0 eV, which establishes a bridge between N-CDs and NiFe-LDH through to facilitate the electron transfer during OER process. It is obvious that pyridinic-N and pyrrolic-N are the two major species to maintain the strong interactions. Furthermore, as shown in Fig. 2(d), C=C/C–C (284.8 eV), C–N/C–OH (286.5 eV), and C=N/C=O (288.8 eV) can be clearly observed in the C 1s region [37]. Similarly, the O 1s region can be simply deconvoluted into three peaks (Fig. S7(b) in the ESM), located at 528.2, 530.7, and 531.7 eV, which are assigned to lattice oxygen (O_L), metal-O (M-O: Ni/Fe-O), and metal-OH (M-OH: Ni/Fe-OH), respectively. As stated above, the strong interaction between NiFe-LDH and N-CDs via M–N–C bond can effectively optimize the electronic structure and simultaneously provide additional active sites, thereby may promoting the OER kinetics and enhancing the catalytic activity.

The performance in OER electrolysis of N-CDs/NiFe-LDH/NF was systematically examined in 1.0 M KOH electrolyte. Figure S8 in the ESM demonstrates LSV curves and Tafel plots of the as-obtained samples with different amounts of N-CDs. Among them, N-CDs/NiFe-LDH/NF (unless otherwise stated, the marked N-CDs/NiFe-LDH/NF in the following discussions just represents N-CDs/NiFe-LDH/NF-0.3) exhibits the best OER electrocatalytic activity and the fastest OER kinetics. It only requires an overpotential of 260 mV to deliver 100 $mA \cdot cm_{geo}^{-2}$, and the Tafel slope is as low as 43.4 $mV \cdot dec^{-1}$. As illustrated in Figs. 3(a) and 3(b), the LSV polarization curves of the as-prepared electrodes, namely, N-CDs/NiFe-LDH/NF, NiFe-LDH/NF, RuO_2/NF, N-

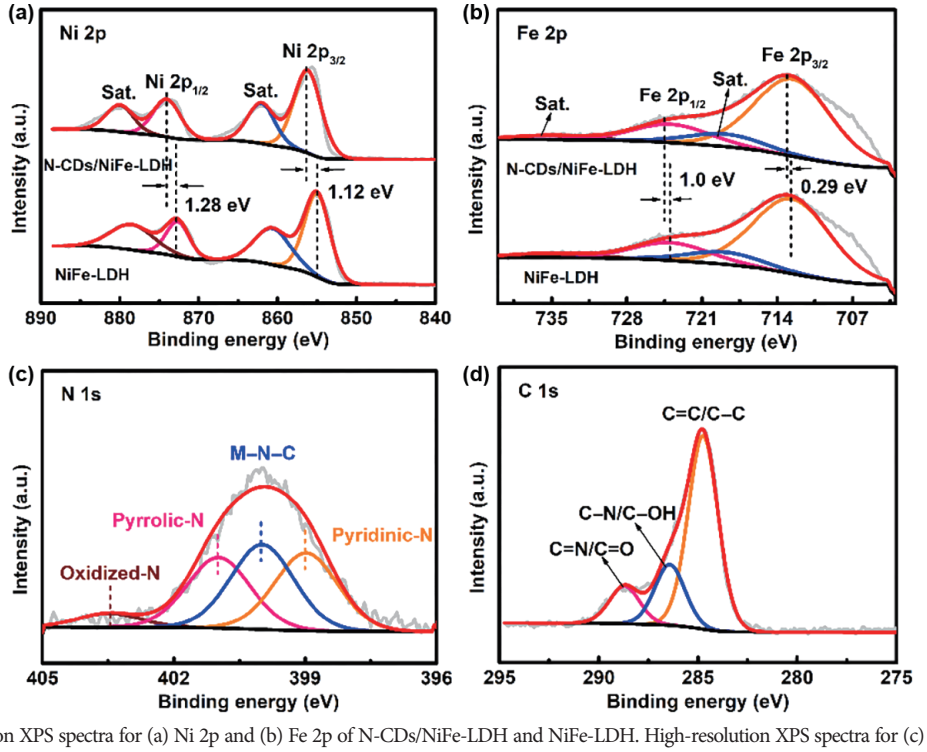

Figure 2 High-resolution XPS spectra for (a) Ni 2p and (b) Fe 2p of N-CDs/NiFe-LDH and NiFe-LDH. High-resolution XPS spectra for (c) N 1s and (d) C 1s of N-CDs/NiFe-LDH.

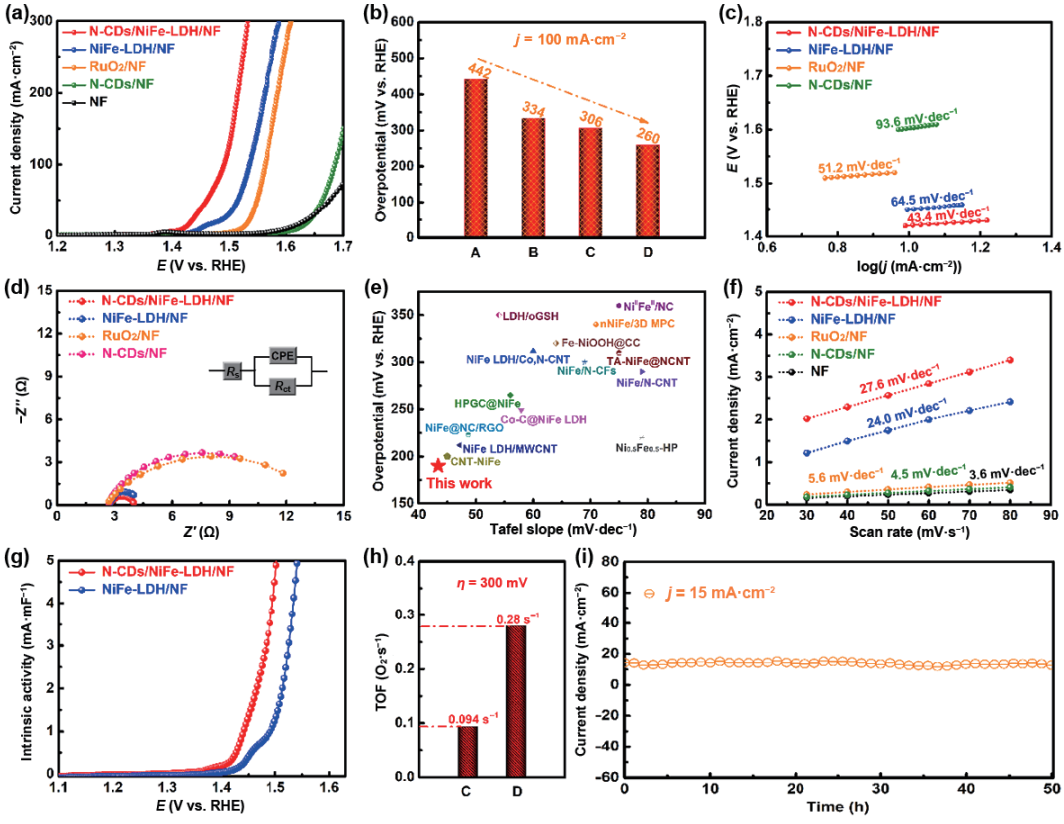

Figure 3 Electrocatalytic OER in 1.0 M KOH: (a) LSV curves of N-CDs/NiFe-LDH/NF, NiFe-LDH/NF, RuO_2/NF, N-CDs/NF, and pure NF. (b) Overpotentials (η) of A, B, C, and D (A = N-CDs/NF, B = RuO_2/NF, C = NiFe-LDH/NF, and D = N-CDs/NiFe-LDH/NF). (c) Tafel slopes, and (d) Nyquist plots of N-CDs/NiFe-LDH/NF, NiFe-LDH/NF, RuO_2/NF, and N-CDs/NF. (e) Overpotentials and Tafel slopes of N-CDs/NiFe-LDH/NF, compared with the results of previously reported OER electrocatalysts. (f) Capacitive currents of the as-prepared samples at 1.375 V vs. RHE as a function of the scan rate. (g) Intrinsic OER catalytic activities of N-CDs/NiFe-LDH/NF and NiFe-LDH/NF after ECSA normalization. (h) TOF at η = 300 mV of C and D (same as C and D in (b)). (i) Time-dependent current density curve at a fixed overpotential of 198 mV for 50 h.

CDs/NF, and pure NF, exhibit significant differences for water oxidation electrocatalytic activity in 1.0 M KOH. By contrast, the N-CDs/NiFe-LDH/NF electrode exhibits the lowest overpotential (η = 260 mV at 100 mA·cm^{-2}), surpassing that of NiFe-LDH/NF, RuO_2/NF, N-CDs/NF, and pure NF. Moreover, Figs. 3(c) and 3(d) show the smallest Tafel slopes and Nyquist plots of various samples, in which the N-CDs/NiFe-LDH/NF electrode displays the smallest Tafel slope of 43.4 mV·dec^{-1} and the lowest charge-transfer resistance (R_{ct} = 1.31 Ω, Table S2 in the ESM), reflecting the favorable OER process. As discussed above, it is demonstrated that the integration of N-CDs with NiFe-LDH enables to enhances the electronic conductivity and accelerate efficient mass transfer, and the outstanding OER performance of N-CDs/NiFe-LDH/NF electrocatalysis is more superior than most of the similar OER catalysts [38–51], as shown in Fig. 3(e).

For a more in-depth understanding of the intrinsic electrocatalytic activity toward water oxidation, the C_{dl} was measured to investigate the ECSA via using a CV test (from 30 to 80 mV·s^{-1} in a nonfaradaic region) in Fig. 3(f) and Fig. S9 in the ESM. The C_{dl} value for N-CDs/NiFe-LDH/NF is 27.6 mF·cm^{-2}, which is the highest C_{dl} value among the as-prepared samples, demonstrating the sufficient exposure of specific surface area and active sites. Similarly, the result shows NiFe-LDH/NF has a C_{dl} value of 24.0 mF·cm^{-2}, which is comparable to that of N-CDs/NiFe-LDH/NF, demonstrating that the active surface area of NiFe-LDH before and after loading N-CDs is relatively identical. Consequently, it can be hypothesized that the improved electrocatalytic activity of N-CDs/NiFe-LDH/NF is attributed to the synergistic effect of the individual components to enhance intrinsic activity. As depicted in Fig. 3(g), even after ECSA normalization, the intrinsic OER catalytic activity (mA·mF^{-1}) of N-CDs/NiFe-LDH/NF and NiFe-LDH/NF still follows the same trend in their overall electrode performance: The N-CDs/NiFe-LDH/NF electrodes are indeed intrinsically more active toward OER than NiFe-LDH/NF. The TOF values of N-CDs/NiFe-LDH/NF and NiFe-LDH/NF are further calculated by normalizing the total number of electrochemically accessible Ni active sites. The TOF values of these two samples still follow the same trend in their intrinsic OER catalytic activity (Fig. S10 in the ESM): N-CDs/NiFe-LDH/NF exhibits a higher TOF value under the same overpotential. As shown in Fig. 3(h), at η = 300 mV, N-CDs/NiFe-LDH/NF reaches a TOF value of 0.28 s^{-1}, which is approximately three-fold higher than that of NiFe-LDH/NF. Furthermore, Fig. S11 in the ESM shows that the mass activity (current density/electrocatalyst loading) of N-CDs/NiFe-LDH/NF (110.1 mA·mg^{-1}, loading: 2.6 mg·cm^{-2}) is about three-fold that of NiFe-LDH/NF (38.3 mA·mg^{-1}, loading: 2.2 mg·cm^{-2}), also further supporting the above results as discussed above.

Furthermore, long-term stability is an important parameter for evaluating the electrocatalyst. As illustrated in Fig. S12 in the ESM, the LSV polarization curves show a slight decay after a 1,000-cycle of CV test for N-CDs/NiFe-LDH/NF, which is coincided with chronoamperometry measurement at an overpotential of 198 mV for an extended reaction time of 50 h (Fig. 3(i)). Impressively, the LSV polarization curves in different electrolytes show almost only extremely slight changes before and after the stability test (Fig. S13 in the ESM). The slight current attenuation in the stability test is attributed to the local acidic environment caused by the N-CDs/NiFe-LDH/NF catalyst can retain an almost stable current trend under stepwise increasing applied voltage, generation of H ions on the surface of the catalyst, which leads to the trace dissolution of active sites in N-CDs/NiFe-LDH/NF [52].

Moreover, Fig. S14 in the ESM displays a multi-step chronopotentiometric curve for N-CDs/NiFe-LDH/NF without iR correction, which shows superior mechanical stability and mass transfer of the catalyst. Subsequently, SEM, XRD, and XPS were also carried out to explore the structural changes of N-CDs/NiFe-LDH/NF after stability testing. The N-CDs/NiFe-LDH/NF electrode shows a rough morphology on the surface of the nanosheets after reaction, while it still maintains the structural characteristics of the nanosheets (Fig. S15 in the ESM). The catalysts show significant changes in phase and composition. In addition to the original N-CDs/NiFe-LDH phase, a new phase appears after the stability test. The diffraction peaks at 18.353°, 37.28°, and 66.761° correspond to the (001), (002), and (110) planes of the new phase γ-NiOOH, respectively (Fig. S16 in the ESM). Moreover, as depicted in Figs. S17(a) and S17(b) in the ESM, the Ni $2p_{3/2}$ and Ni $2p_{1/2}$ peaks in N-CDs/NiFe-LDH/NF shift to higher binding energy in comparison with the initial one, while Fe 2p shows almost no obvious change, demonstrating the improved oxidation state after OER. As further observed in Figs. S17(c) and S17(d) in the ESM, the signal assigned to the M–O of oxyhydroxides significantly increases, indicative of the generation of high-valence-state nickel species (e.g., $Ni(OH)_2$ → γ-NiOOH), further consisting with the oxidation reaction of Ni^{2+}/Ni^{3+} [53], as exhibited in the LSV polarization curves.

To further broaden the practical application environment of N-CDs/NiFe-LDH/NF, the OER activity of N-CDs/NiFe-LDH/NF was also evaluated in simulated seawater (1.0 M KOH + 0.5 M/1.0 M NaCl) and alkaline seawater (1.0 M KOH + seawater) electrolytes. As illustrated Figs. 4(a) and 4(b), the three LSV curves of N-CDs/NiFe-LDH/NF display nearly the same trend no matter whether Cl^- exists or not, due to the very low overpotential of below 480 mV, which is not big enough to trigger the ClOR, so as to achieve 100% seawater electrolysis. Furthermore, the OER activity of the N-CDs/NiFe-LDH/NF catalyst still performs well with only a slight decay in the real seawater electrolyte, requiring only 340 mV to drive 100 mA·cm^{-2}, as illustrated in Fig. 4(c). The peak caused by a large current increase can be observed in the LSV curve at about 1.46 V, which is derived from the oxidation reaction of Ni^{2+}/Ni^{3+}. As we know, the source of catalyst activity decay is inseparable from the complex environment of real seawater. Various species (e.g., microorganisms, organic, and inorganic impurities) present in real seawater can easily cause catalyst poisoning, and gradually form insoluble precipitates covering the surface of the catalyst during OER operation, resulting in the inability of some active sites to play a catalytic role [54]. In spite of this, N-CDs/NiFe-LDH/NF can still maintain the current density of 10 mA·cm^{-2} for 20 h in both the simulated and alkaline seawater electrolytes without significant attenuation as shown in Figs. 4(d)–4(f), indicating that the existing chloride-containg species have no significant poison effect on the active sites mainly due to superior performance of N-CDs/NiFe-LDH/NF with a low overpotential.

4 Conclusions

In summary, we have proposed a facile strategy to fabricate robust and stable catalysts for electrocatalytic alkaline water and seawater oxidation, in which NiFe-LDH was modified by N-CDs to form M–N–C bonding to promote the charge transfer process and improve the intrinsic activity. Attributed to the strong coupled interaction between the composite components and optimized electronic structures in the hybrids, the well fabricated N-CDs/NiFe-LDH/NF effectively precludes the chloride ion from corroding the electrode, resulting in the excellent electrocatalytic performance in both 1.0 M KOH and simulated seawater electrolyte. Briefly, N-CDs/NiFe-LDH/NF shows a low overpotential of only 260 mV (1.0 M KOH), 285 mV, and 273 mV (1.0 M KOH + 0.5 M/1.0 M NaCl) at 100 mA·cm^{-2} for the electrolytic OER process, respectively. Also, such a catalyst could resist the poisoning reaction caused by the complex environment of real seawater, and still exert high catalytic activity to deliver 100 mA·cm^{-2} at a low overpotential of 340 mV, which well avoids triggering ClOR. Furthermore, N-CDs/NiFe-LDH/NF displays long-term durability within dozens of hours in both 1.0 M KOH and alkaline seawater splitting. Overall, this work may shed a new light on the fabrication of robust catalysts for seawater oxidation, and it is envisioned that the design concept can inspire the research and development of carbon-based materials with excellent OER performance.

Acknowledgements

This work was supported by the National Natural Science Foundation of China (Nos. 52122308, 21905253, and 51973200), and the Natural Science Foundation of Henan (No. 202300410372).

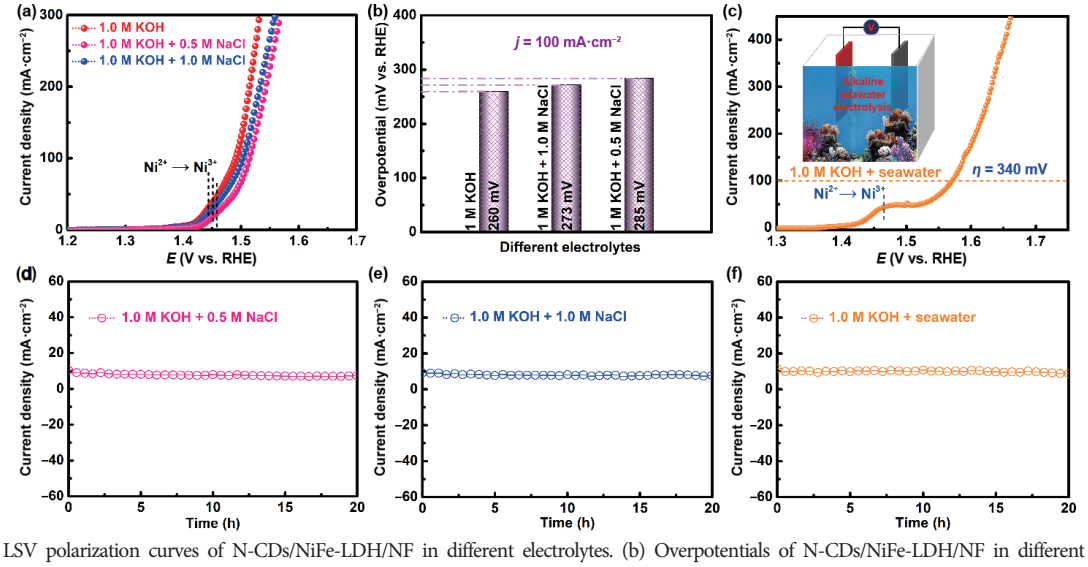

Figure 4 (a) LSV polarization curves of N-CDs/NiFe-LDH/NF in different electrolytes. (b) Overpotentials of N-CDs/NiFe-LDH/NF in different electrolytes at 100 mA·cm^{-2}. (c) LSV polarization curves of N-CDs/NiFe-LDH/NF in alkaline seawater electrolyte (inset: schematic diagram of electrolytic cell). (d)–(f) The stability test of N-CDs/NiFe-LDH/NF in simulated and alkaline seawater electrolytes.

Electronic Supplementary Material: Supplementary material (SEM images, TEM images, XPS spectrum, XRD patterns, LSV curves, Tafel plots, cyclic voltammograms, TOF curves, mass activity curves, multi-step chronopotentiometric curve, and Tables S1 and S2 in the ESM) is available in the online version of this article at https://doi.org/10.1007/s12274-022-4377-4.

References

[1] Zhou, D. J.; Li, P. S.; Lin, X.; McKinley, A.; Kuang, Y.; Liu, W.; Lin, W. F.; Sun, X. M.; Duan, X. Layered double hydroxide-based electrocatalysts for the oxygen evolution reaction: Identification and tailoring of active sites, and superaerophobic nanoarray electrode assembly. *Chem. Soc. Rev.* **2021**, *50*, 8790–8817.

[2] Shi, Z. P.; Wang, Y.; Li, J.; Wang, X.; Wang, Y. B.; Li, Y.; Xu, W. L.; Jiang, Z.; Liu, C. P.; Xing W. et al. Confined Ir single sites with triggered lattice oxygen redox: Toward boosted and sustained water oxidation catalysis. *Joule* **2021**, *5*, 2164–2176.

[3] Zhang, N.; Chai, Y. Lattice oxygen redox chemistry in solid-state electrocatalysts for water oxidation. *Energy Environ. Sci.* **2021**, *14*, 4647–4671.

[4] Wang, J.; Kim, S. J.; Liu, J. P.; Gao, Y.; Choi, S.; Han, J.; Shin, H.; Jo, S.; Kim, J.; Ciucci, F. et al. Redirecting dynamic surface restructuring of a layered transition metal oxide catalyst for superior water oxidation. *Nat. Catal.* **2021**, *4*, 212–222.

[5] Chang, J. W.; Yu, C.; Song, X. D.; Tan, X. Y.; Ding, Y. W.; Zhao, Z. B.; Qiu, J. S. A C-S-C linkage-triggered ultrahigh nitrogen-doped carbon and the identification of active site in triiodide reduction. *Angew. Chem., Int. Ed.* **2021**, *60*, 3587–3595.

[6] Souza, A. S.; Bezerra, L. S.; Cardoso, E. S. F.; Fortunato, G. V.; Maia, G. Nickel pyrophosphate combined with graphene nanoribbon used as efficient catalyst for OER. *J. Mater. Chem. A* **2021**, *9*, 11255–11267.

[7] Tang, T. M.; Zhang, Q. Q.; Bai, X.; Wang, Z. L.; Guan, J. P. Enhanced oxygen evolution activity on mesoporous cobalt-iron oxides. *Chem. Commun.* **2021**, *57*, 11843–11846.

[8] Fan, Y. X.; Zhang, X. D.; Zhang, Y. J.; Xie, X.; Ding, J.; Cai, J. L.; Li, B. J.; Lv, H. L.; Liu, L. Y.; Zhu, M. M. et al. Decoration of Ru/RuO_2 hybrid nanoparticles on MoO_2 plane as bifunctional electrocatalyst for overall water splitting. *J. Colloid Interface Sci.* **2021**, *604*, 508–516.

[9] Bahadur, A.; Hussain, W.; Iqbal, S.; Ullah, F.; Shoaib, M.; Liu, G. C.; Feng, K. J. A morphology controlled surface sulfurized $CoMn_2O_4$ microspike electrocatalyst for water splitting with excellent OER rate for binder-free electrocatalytic oxygen evolution. *J. Mater. Chem. A* **2021**, *9*, 12255–12264.

[10] Chen, Y. Y.; Xu, Y.; Niu, S.; Yan, J.; Wu, Y. Y.; Du, F. K.; Zhao, Y. Z.; Zhu, Z. R.; Jiang, Z. J.; Tan, X. C. A highly efficient Fe-Ni-S/NF hybrid electrode for promoting oxygen evolution performance. *Chem. Commun.* **2021**, *57*, 4572–4575.

[11] Song, H. Q.; Wu, M.; Tang, Z. Y.; Tse, J. S.; Yang, B.; Lu, S. Y. Single atom ruthenium-doped CoP/CDs nanosheets via splicing of carbon-dots for robust hydrogen production. *Angew. Chem., Int. Ed.* **2021**, *60*, 7234–7244.

[12] Zhang, F. H.; Yu, L.; Wu, L. B.; Luo, D.; Ren, Z. F. Rational design of oxygen evolution reaction catalysts for seawater electrolysis. *Trends Chem.* **2021**, *3*, 485–498.

[13] Chang, J. F.; Wang, G. Z.; Yang, Z. Z.; Li, B. Y.; Wang, Q.; Kuliiev, R.; Orlovskaya, N.; Gu, M.; Du, Y. G.; Wang, G. F. et al. Dual-doping and synergism toward high-performance seawater electrolysis. *Adv. Mater.* **2021**, *33*, 2101425.

[14] Yu, L.; Wu, L. B.; McElhenny, B.; Song, S. W.; Luo, D.; Zhang, F. H.; Yu, Y.; Chen, S.; Ren, Z. F. Ultrafast room-temperature synthesis of porous S-doped Ni/Fe (oxy) hydroxide electrodes for oxygen evolution catalysis in seawater splitting. *Energy Environ. Sci.* **2020**, *13*, 3439–3446.

[15] Yu, Z. Y.; Duan, Y.; Feng, X. Y.; Yu, X. X.; Gao, M. R.; Yu, S. H. Clean and affordable hydrogen fuel from alkaline water splitting: Past, recent progress, and future prospects. *Adv. Mater.* **2021**, *33*, 2007100.

[16] Xiang, K.; Song, Z. X.; Wu, D.; Deng, X. H.; Wang, X. W.; You, W.; Peng, Z. K.; Wang, L.; Luo, J. L.; Fu, X. Z. Bifunctional Pt-Co_3O_4 electrocatalysts for simultaneous generation of hydrogen and formate via energy-saving alkaline seawater/methanol co-electrolysis. *J. Mater. Chem. A* **2021**, *9*, 6316–6324.

[17] Hu, Y. M.; Liu, W. J.; Jiang, K.; Xu, L.; Guan, M. L.; Bao, J.; Ji, H. B.; Li, H. M. Constructing a CeO_{2-x}@CoFe-layered double hydroxide heterostructure as an improved electrocatalyst for highly efficient water oxidation. *Inorg. Chem. Front.* **2020**, *7*, 4461–4468.

[18] Chen, H. J.; Zou, Y. H.; Li, J.; Zhang, K. W.; Xia, Y. Z.; Hui, B.; Yang, D. J. Wood aerogel-derived sandwich-like layered nanoelectrodes for alkaline overall seawater electrosplitting. *Appl. Catal. B:Environ.* **2021**, *293*, 120215.

[19] Zhou, L.; Zhang, C.; Zhang, Y. Q.; Li, Z. H.; Shao, M. F. Host modification of layered double hydroxide electrocatalyst to boost the thermodynamic and kinetic activity of oxygen evolution reaction. *Adv. Funct. Mater.* **2021**, *31*, 2009743.

[20] Dresp, S.; Dionigi, F.; Klingenhof, M.; Merzdorf, T.; Schmies, H.; Drnec, J.; Poulain, A.; Strasser, P. Molecular understanding of the impact of saline contaminants and alkaline pH on NiFe layered double hydroxide oxygen evolution catalysts. *ACS Catal.* **2021**, *11*, 6800–6809.

[21] Chen, W.; Wu, B. B.; Wang, Y. Y.; Zhou, W.; Li, Y. Y.; Liu, T. Y.; Xie, C.; Xu, L. T.; Du, S. Q.; Song, M. L. et al. Deciphering the alternating synergy between interlayer Pt single-atom and NiFe layered double hydroxide for overall water splitting. *Energy Environ. Sci.* **2021**, *14*, 6428–6440.

[22] Peng, L. S.; Yang, N.; Yang, Y. Q.; Wang, Q.; Xie, X. Y.; Sun-Waterhouse, D.; Shang, L.; Zhang, T. R.; Waterhouse, G. I. N. Atomic cation-vacancy engineering of NiFe-layered double hydroxides for improved activity and stability towards the oxygen evolution reaction. *Angew. Chem., Int. Ed.* **2021**, *60*, 24612–24619.

[23] Ding, P.; Meng, C. Q.; Liang, J.; Li, T. S.; Wang, Y.; Liu, Q.; Luo, Y. L.; Cui, G. W.; Asiri, A. M.; Lu, S. Y. et al. NiFe layered-double-hydroxide nanosheet arrays on graphite felt: A 3D electrocatalyst for highly efficient water oxidation in alkaline media. *Inorg. Chem.* **2021**, *60*, 12703–12708.

[24] Chen W. Z.; Zhang M.; Liu Y.; Yao X.; Liu P. Y.; Liu Z. L.; He J. L.; Wang Y. Q. Super-hydrophilic MgO/$NiCo_2S_4$ heterostructure for high-efficient oxygen evolution reaction in neutral electrolytes.. *Appl. Catal. B: Environ.* **2022**, *312*–121432.

[25] Ji, X. X.; Lin, Y. H.; Zeng, J.; Ren, Z. H.; Lin, Z. J.; Mu, Y. B.; Qiu, Y. J.; Yu, J. Graphene/MoS_2/FeCoNi $(OH)_x$ and graphene/MoS_2/$FeCoNiP_x$ multilayer-stacked vertical nanosheets on carbon fibers for highly efficient overall water splitting. *Nat. Commun.* **2021**, *12*, 1380.

[26] Liu, H.; Liu, Z. H.; Wang, Y.; Zhang, J. Q.; Yang, Z. X.; Hu, H.; Zhao, Q. S.; Ning, H.; Zhi, L. J.; Wu, M. B. Carbon dots-oriented synthesis of fungus-like CoP microspheres as a bifunctional electrocatalyst for efficient overall water splitting. *Carbon* **2021**, *182*, 327–334.

[27] Yang, M. X.; Feng, T. L.; Chen, Y. X.; Liu, J. J.; Zhao, X. H.; Yang, B. Synchronously integration of Co, Fe dual-metal doping in Ru@C and CDs for boosted water splitting performances in alkaline media. *Appl. Catal. B:Environ.* **2020**, *267*, 118657.

[28] Chang, J. W.; Song, X. D.; Yu, C.; Huang, H. W.; Hong, J. F.; Ding, Y. W.; Huang, H. L.; Yu, J. H.; Tan, X. Y.; Zhao, Z. B. et al. Gravity field-mediated synthesis of carbon-conjugated quantum dots with tunable defective density for enhanced triiodide reduction. *Nano Energy* **2020**, *69*, 104377.

[29] Yu, J. K.; Song, H. Q.; Li, X.; Tang, L.; Tang, Z. Y.; Yang, B.; Lu, S. Y. Computational studies on carbon dots electrocatalysis: A review. *Adv. Funct. Mater.* **2021**, *31*, 2107196.

[30] Song, H. Q.; Cheng, Y. J.; Li, B. J.; Fan, Y. P.; Liu, B. Z.; Tang, Z. Y.; Lu, S. Y. Carbon dots and RuP_2 nanohybrid as an efficient bifunctional catalyst for electrochemical hydrogen evolution reaction and hydrolysis of ammonia borane. *ACS Sustainable Chem. Eng.* **2020**, *8*, 3995–4002.

[31] Gu, X. Q.; Chen, Z. M.; Li, Y.; Wu, J.; Wang, X.; Huang, H.; Liu, Y.; Dong, B.; Shao, M. W.; Kang, Z. H. Polyaniline/carbon dots composite as a highly efficient metal-free dual-functional

photoassisted electrocatalyst for overall water splitting. *ACS Appl. Mater. Interfaces* **2021**, *13*, 24814–24823.

[32] Liu, Y. H.; Ge, R. Y.; Chen, Y. Y.; Huang, M. Q.; Zhu, R. J.; Li, W. X.; Liu, Y.; Feng, L. Y.; Che, R. C. Urchin-like cobalt hydroxide coupled with N-doped carbon dots hybrid for enhanced electrocatalytic water oxidation. *Chem. Eng. J.* **2021**, *420*, 127598.

[33] Feng, T. L.; Zeng, Q. S.; Lu, S. Y.; Yang, M. X.; Tao, S. Y.; Chen, Y. X.; Zhao, Y.; Yang, B. Morphological and interfacial engineering of cobalt-based electrocatalysts by carbon dots for enhanced water splitting. *ACS Sustainable Chem. Eng.* **2019**, *7*, 7047–7057.

[34] Wang, L.; Wen, Y. Z.; Ji, Y. J.; Cao, H. J.; Li, S. Y.; He, S. S.; Bai, H. P.; Liu, G. J.; Zhang, L. S.; Bao, H. L. et al. The 3d–5d orbital repulsion of transition metals in oxyhydroxide catalysts facilitates water oxidation. *J. Mater. Chem. A* **2019**, *7*, 14455–14461.

[35] Wang, Z. P. ; Zhang, J. H. ; Yu, Q. Y. ; Yang, H. Y. ; Chen, X. ; Yuan, X. ; Huang, K. ; Xiong, X. L. Synthesis of 3D CoO nanowires supported NiFe layered double hydroxide using an atmospheric pressure microplasma for high-performance oxygen evolution reaction. *Chem. Eng. J.* **202**1, *410*, 128366.

[36] Chang, J. W.; Song, X. D.; Yu, C.; Yu, J. H.; Ding, Y. W.; Yao, C.; Zhao, Z. B.; Qiu, J. S. Hydrogen-bonding triggered assembly to configure hollow carbon nanosheets for highly efficient Tri-iodide reduction. *Adv. Funct. Mater.* **2020**, *30*, 2006270.

[37] Sun, C. B.; Ding, J.; Wang, H. Z.; Liu, J.; Han, X. P.; Deng, Y. D.; Zhong, C.; Hu, W. B. Cobalt sulfides constructed heterogeneous interfaces decorated on N, S-codoped carbon nanosheets as a highly efficient bifunctional oxygen electrocatalyst. *J. Mater. Chem. A* **2021**, *9*, 13926–13935.

[38] Wang, W.; Liu, Y. C.; Li, J.; Luo, J.; Fu, L.; Chen, S. L. NiFe LDH nanodots anchored on 3D macro/mesoporous carbon as a high-performance ORR/OER bifunctional electrocatalyst. *J. Mater. Chem. A* **2018**, *6*, 14299–14306.

[39] Wang, Q.; Shang, L.; Shi, R.; Zhang, X.; Zhao, Y. F.; Waterhouse, G. I. N.; Wu, L. Z.; Tung, C. H.; Zhang, T. R. NiFe layered double hydroxide nanoparticles on Co, N-codoped carbon nanoframes as efficient bifunctional catalysts for rechargeable zinc-air batteries. *Adv. Energy Mater.* **2017**, *7*, 1700467.

[40] Li, W. M.; Chen, S. H.; Zhong, M. X.; Wang, C.; Lu, X. F. Synergistic coupling of NiFe layered double hydroxides with Co-C nanofibers for high-efficiency oxygen evolution reaction. *Chem. Eng. J.* **2021**, *415*, 128879.

[41] Ni, Y. M.; Yao, L. H.; Wang, Y.; Liu, B.; Cao, M. H.; Hu, C. W. Construction of hierarchically porous graphitized carbon-supported NiFe layered double hydroxides with a core–shell structure as an enhanced electrocatalyst for the oxygen evolution reaction. *Nanoscale* **2017**, *9*, 11596–11604.

[42] Liu, X. J.; Li, S. Z.; Akinwolemiwa, B.; Hu, D.; Wu, T.; Peng, C. Low-crystalline transition metal oxide/hydroxide on MWCNT by Fenton-reaction-inspired green synthesis for lithium ion battery and OER electrocatalysis. *Electrochim. Acta* **2021**, *387*, 138559.

[43] Lei, H.; Wang, Z. L.; Yang, F.; Huang, X. Q.; Liu, J. H.; Liang, Y. Y.; Xie, J. P.; Javed, M. S.; Lu, X. H.; Tan, S. Z. et al. NiFe nanoparticles embedded N-doped carbon nanotubes as high-efficient electrocatalysts for wearable solid-state Zn-air batteries. *Nano Energy* **2020**, *68*, 104293.

[44] Xie, X. Y.; Shang, L.; Shi, R.; Waterhouse, G. I. N.; Zhao, J. Q.; Zhang, T. R. Tubular assemblies of N-doped carbon nanotubes loaded with NiFe alloy nanoparticles as efficient bifunctional catalysts for rechargeable zinc-air batteries. *Nanoscale* **2020**, *12*, 13129–13136.

[45] Li, Y. M.; He, H. Y.; Fu, W.; Mu, C. Z.; Tang, X. Z.; Liu, Z.; Chi. D. Z.; Hu, X. In-grown structure of NiFe mixed metal oxides and CNT hybrid catalysts for oxygen evolution reaction. *Chem. Commun.* **2016**, *52*, 1439–1442.

[46] Niu, Y. L.; Teng, X.; Gong, S. Q.; Chen, Z. F. A bimetallic alloy anchored on biomass-derived porous N-doped carbon fibers as a self-supporting bifunctional oxygen electrocatalyst for flexible Zn-air batteries. *J. Mater. Chem. A* **2020**, *8*, 13725–13734.

[47] Yue, X. Y.; Song, C. S.; Yan, Z. Y.; Shen, X. P.; Ke, W. T.; Ji, Z. Y.; Zhu, G. X.; Yuan, A. H.; Zhu, J.; Li, B. L. Reduced graphene oxide supported nitrogen-doped porous carbon-coated NiFe alloy composite with excellent electrocatalytic activity for oxygen evolution reaction. *Appl. Surf. Sci.* **2019**, *493*, 963–974.

[48] Yi, L. Y.; Niu, Y. L.; Feng, B. M.; Zhao, M.; Hu, W. H. Simultaneous phase transformation and doping via a unique photochemical-electrochemical strategy to achieve a highly active Fe-doped Ni oxyhydroxide oxygen evolution catalyst. *J. Mater. Chem. A* **2021**, *9*, 4213–4220.

[49] Qiao, H. Y.; Yang, Y.; Dai, X. P.; Zhao, H. H.; Yong, J. X.; Yu, L.; Luan, X. B.; Cui, M. L.; Zhang, X.; Huang, X. L. Amorphous (Fe) Ni-MOF-derived hollow (bi) metal/oxide@N-graphene polyhedron as effectively bifunctional catalysts in overall alkaline water splitting. *Electrochim. Acta* **2019**, *318*, 430–439.

[50] Zhu, X. L.; Tang, C.; Wang, H. F.; Zhang, Q.; Yang, C. H.; Wei, F. Dual-sized NiFe layered double hydroxides *in situ* grown on oxygen-decorated self-dispersal nanocarbon as enhanced water oxidation catalysts. *J. Mater. Chem. A* **2015**, *3*, 24540–24546.

[51] Du, L.; Luo, L. L.; Feng, Z. X.; Engelhard, M.; Xie, X. H.; Han, B. H.; Sun, J. M.; Zhang, J. H.; Yin, G. P.; Wang, C. M. et al. Nitrogen-doped graphitized carbon shell encapsulated NiFe nanoparticles: A highly durable oxygen evolution catalyst. *Nano Energy* **2017**, *39*, 245–252.

[52] Chen, R.; Hung, S. F.; Zhou, D. J.; Gao, J. J.; Yang, C. J.; Tao, H. B.; Yang, H. B.; Zhang, L. P.; Zhang, L. L.; Xiong, Q. H. et al. Layered structure causes bulk NiFe layered double hydroxide unstable in alkaline oxygen evolution reaction. *Adv. Mater.* **2019**, *31*, 1903909.

[53] Zhou, Y.; Zhang, W. B.; Hu, J. L.; Li, D.; Yin, X.; Gao, Q. S. Inherent oxygen vacancies boost surface reconstruction of ultrathin Ni-Fe layered-double-hydroxides toward efficient electrocatalytic oxygen evolution. *ACS Sustainable Chem. Eng.* **2021**, *9*, 7390–7399.

[54] Wang, X. H.; Ling, Y.; Wu, B.; Li, B. L.; Li, X. L.; Lei, J. L.; Li, N. B.; Luo, H. Q. Doping modification, defects construction, and surface engineering: Design of cost-effective high-performance electrocatalysts and their application in alkaline seawater splitting. *Nano Energy* **2021**, *87*, 106160.